Wireless Signaling of Beta Detection Using Microdischarges

Christine K. Eun, Ranjit Gharpurey, and Yogesh B. Gianchandani, *Senior Member, IEEE*

***Abstract*—This paper explores the possibility of using microdischarges to generate broadband radio-frequency (RF) signaling from gas-based microdetectors of beta radiation. The concept is evaluated using two types of lithographically manufactured test structures: 1) a silicon/glass stack with etched detection cavities and 2) a planar metal-on-glass structure. The test structures include electrodes that bias a fill-gas region with a high electric field, in which incident beta particles initiate avalanche-driven microdischarge pulses that inherently transmit RF spectra with frequency content extending into the ultrawideband (UWB) range of communication. The discharge gaps range from 165 to 500 μm. The impact of operating pressure, fill gases (which are typically a mixture of Ne and N_2), and electrode materials (Ni and Cu) on operating voltage and wireless signaling performance is evaluated. Tests are performed in the proximity of weak (0.1–1.0-μCi) beta sources (^{90}Sr and ^{204}Tl). Both types of test structures are capable of producing UWB signals spanning $>$ 1 GHz. Measurements in an anechoic chamber using various receiver antennas show that microdischarges can produce field strengths up to 90 dB $\cdot$ μV/m measured at 1.67 m from the test structure. [2010-0058]**

***Index Terms*—Gas discharges, nuclear radiation, radio-frequency (RF) signaling, ultrawideband (UWB).**

I. Introduction

MICRODISCHARGES have found applications in a variety of contexts related to microsystems, ranging from manufacturing technologies, e.g., micro-electro-discharge machining (μEDM) and vacuum packaging [1]–[4], to environmental sensing applications, e.g., chemical analysis of fluids and radiation monitoring [5]–[8]. In this effort, we are particularly interested in microdischarge-based radiation detectors, such as Geiger counters. Generally simple and reliable, these devices operate over a large temperature range and can detect a wide range of radiation species and energies. Geiger counters are often the preferred instruments for detecting beta radiation in the field [9]. (Beta detection is useful because the vast majority of hazardous radioisotopes emit beta particles during their decay process.)

Manuscript received March 4, 2010; revised May 20, 2010; accepted June 17, 2010. Date of publication July 21, 2010; date of current version July 30, 2010. This work was supported in part by the Engineering Research Centers Program of the National Science Foundation under Award EEC-9986866 and in part by the U.S. Army Research Laboratory Micro Autonomous Systems and Technology Collaborative Technology Alliance. Subject Editor N. F. de Rooij.

C. K. Eun and Y. B. Gianchandani are with the Department of Electrical Engineering and Computer Science, University of Michigan, Ann Arbor, MI 48109 USA (e-mail: eunc@umich.edu).

R. Gharpurey is with the Department of Electrical and Computer Engineering, University of Texas at Austin, TX 78712 USA.

Color versions of one or more of the figures in this paper are available online at http://ieeexplore.ieee.org.

Digital Object Identifier 10.1109/JMEMS.2010.2055546

Almost all gas-based radiation detectors utilize a pair of biased electrodes immersed within a fill gas. Radiation-induced ionization of gas molecules leads to current that can be amplified to varying levels by the applied bias. At the lowest bias level, known as the ion saturation regime, the population of ionized carriers equals the amount directly produced by the radiation. At a higher biasing level, known as the proportional regime, the number of carriers is amplified by the avalanche but remains proportional to the amount originally produced. At the highest bias level, known as the Geiger–Mueller regime, the carrier count reaches a maximum. Each radiation particle, regardless of energy, creates a similar count of carriers, providing signal amplification at the cost of information about the energy spectrum.

Past work in micropatterned gas-based radiation detectors utilized lithographic microfabrication techniques for enhancing the areal density of electrodes and maintaining the precision and accuracy of the interelectrode spacing [10]–[16]. The majority of these detectors were employed in high-energy physics for particle tracking, medical diagnostics for X-ray imaging, or plasma diagnostics. These detectors were typically operated in the proportional regime.

The goal of the work described in this paper is to evaluate wireless signals that are produced by detectors that are typically biased in the Geiger–Mueller regime. It is generally known that radio-frequency (RF) signals can be generated concomitantly with a current discharge. The wireless spectrum, which may extend into the ultrawideband (UWB) frequency range, is dependent on the shape of the current waveform in the time domain [17]–[20]. The radiated electric fields in the near field are governed by the time-domain current behavior, while the far field is controlled by the derivative of the current (based on a $\lambda/2\pi$ transition point) [19].

Historically, the use of electrical discharges to wirelessly transmit information was first employed by Marconi. Building on the foundation of the work developed by Maxwell and Hertz, Marconi utilized electromagnetic emissions produced by spark gaps in his design of the radio transmitter [21]. Spark gaps consist of two conducting electrodes surrounded by some background gas (usually air). The resulting UWB wireless signal can travel over large distances (on the order of kilometers). Efforts to use discharges within waveguides in order to generate microwaves date back to Bose in 1901, and more recent activities have been reported by others [22], [23].

Miniaturized radiation sensors with wireless signaling capability can be useful both individually and in networks. Individually, the devices can be used in applications for which the weight or space is at a premium, e.g., micro air vehicles or

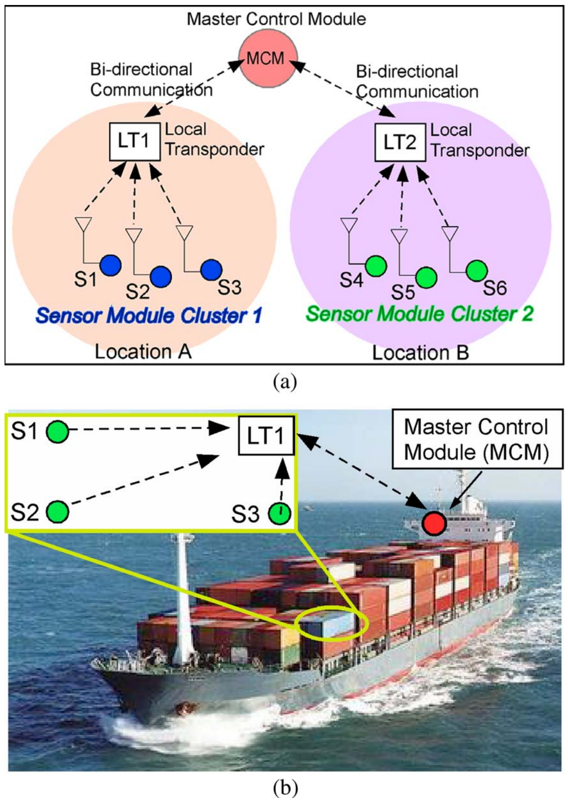

Fig. 1. (a) Possible network configuration plan includes multiple clusters of wireless sensor modules transmitting to an LT that has bidirectional communication capability with the MCM. Each sensor module $(S1, S2, S3, \ldots)$ can transmit on identical frequency bands, which allows instantaneous changes in cluster size and configuration without changes to the LT or MCM. (b) Network configuration plan applied to a cargo container ship scenario.

helmets. As elements of a network, these devices can facilitate discreet, rapid, and cost-effective deployment in public spaces (e.g., football stadia, amusement parks, and shopping malls) or in dangerous and inaccessible environments (e.g., contaminated or remote areas). In one possible configuration [Fig. 1(a)], the wireless microsensors are distributed in clusters—locations A, B, etc. Within each cluster, there are a number of functionally identical individual sensors that are interchangeable, transmitting on the same frequency bands. Each cluster communicates to a localized transponder (LT), which reports to a centralized master control module (MCM). A possible application is the monitoring of a large cargo ship [Fig. 1(b)], with each shipping container housing a sensor cluster and an LT and with the MCM being located at the helm. In general, such devices promise high portability, minimal power demands, and modest manufacturing costs.

Past work on wireless-enabled detector networks has included the use of multiple 75-mm NaI scintillators connected to personal digital assistant-sized platforms that are linked to mote gateways [24], and arrays of $2'' \times 2''$ radiation detectors communicating via wireless mesh routing protocols [25]. Both require radiation-shielded transponders at each sensor node. Offering inherent signaling capabilities for each sensor can simplify the nodes and reduce the overall sensor cost.

In this paper, we examine gas-based microdetectors and the inherent wireless transmissions that can be generated during sensor operation. Two types of lithographically fabricated test structures are evaluated[1]: 1) a silicon and glass (SiG) micromachined structure with 500-μm discharge gaps and 2) a planar metal-on-glass (MOG) structure with discharge gaps ranging from 165 to 235 μm. Section II describes the method for sensing beta radiation and factors that impact discharge-based wireless signaling. Section III details the fabrication process for the test structures, followed by the experimental results in Section IV. These include both wired measurements of terminal currents and wireless measurements of the transmitted spectrum. The impact of structural variables of the test structure, such as electrode gap, fill gas type, and pressure, is described.

II. Test Structure Operation and Design

This section describes the SiG and MOG test structures introduced earlier and identifies how the design can affect wireless signaling.

A. SiG Test Structure

The SiG structure [Fig. 2(a)] has a gas-filled cavity with two regions that are intended to have very different electric fields: The region proximal to the cathode has a weak field and is called the drift region, whereas that adjacent to the anode is the high-field amplification region. Incident beta particles enter the cavity and ionize the fill gas. (In contrast with conventional Geiger counters, which operate in partial vacuum, this fill gas is near atmospheric pressure, which increases the number of gas molecules that are able to participate in the sensing of radiation.) The ionized carriers within the drift region are moved into the amplification region. In the amplification region, the electrons are quickly accelerated, resulting in an electron cascade and, eventually, a microdischarge. The drift region is designed to be much larger than the amplification region to allow pulses to be relatively independent of the entry position of the beta particle.

The cavity structure comprises a square micromachined Si wall (i.e., the anode) bonded to a glass substrate. The Si wall has two layers: a 22-μm-tall layer of boron-doped p^{++} Si and, above this, a 473-μm-tall layer of bulk Si. In the center of the cavity, there is a square 22-μm-tall p^{++} Si island (i.e., the cathode). The amplification region (approximately 500 μm long) is defined by the p^{++} Si layers of the anode wall and the edge of the cathode. The drift region is located between the center of the cathode and the anode wall and is approximately 4 mm long. The interaction volume, which is defined by the drift and amplification regions, measures 8×8 mm^2 with a depth of approximately 473 μm.

B. MOG Test Structure

The MOG test structure is simpler than the SiG structure, comprising only planar thin-film metal electrodes patterned on a glass substrate [Fig. 2(b)]. The electric field extends between

[1]Portions of this paper have been reported in conference abstract form in [26]–[28].

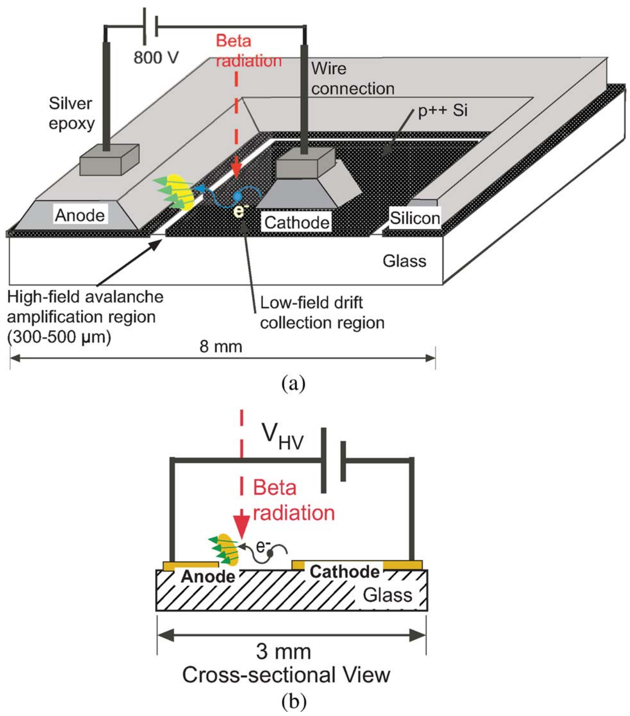

Fig. 2. Each test structure includes a pair of lithographically fabricated electrodes (Si or metal) on a glass substrate. Electrode gaps range from 200 to 500 μm. (a) SiG design has a central cathode and a concentric anode. Beta radiation passing through the weak-field (drift) region near the cathode ionizes the fill gas; the electrons travel to the high-field amplification region near the anode where they are accelerated, creating a current pulse. (b) MOG design is a simpler structure with a single-field region.

the electrodes and in the gas volume immediately above, where the beta-initiated ionization takes place. Various metals can be used for the electrodes—e.g., Cu, Ni, or Ir. The structure with Cu electrodes utilizes a 25-μm-thick layer of metal electroplated on a 500-μm-thick glass substrate. The electrode gaps range from 165 to 235 μm. The interaction volume (i.e., the region between the anode and the cathode) is approximately $200 \times 500\ \mu\text{m}^2$ with a depth of approximately 25–50 μm, as determined by the electric field.

C. Wireless Signaling From Microdischarges

Studies on the discharge characteristics (with electrode gaps from 100 to 500 μm) have shown that the spectral performance can be impacted by several factors, such as electrode gap and electrode capacitance [18]. Smaller electrode gaps (which typically allow lower operating voltages) provide smaller rise/fall times of the discharge current, which increase the bandwidth of the frequency spectrum. The electrode capacitance includes both the parasitic capacitance between the metal electrodes and the space charge surrounding the electrodes. Increasing this capacitance reduces the time derivative (steepness) of the discharge current pulse. (This can be interpreted as the increase in time necessary to transport the charge associated with the larger capacitance.) In the frequency domain, as the electrode capacitance increases, the lower end of the radiated spectrum tends to dominate [18].

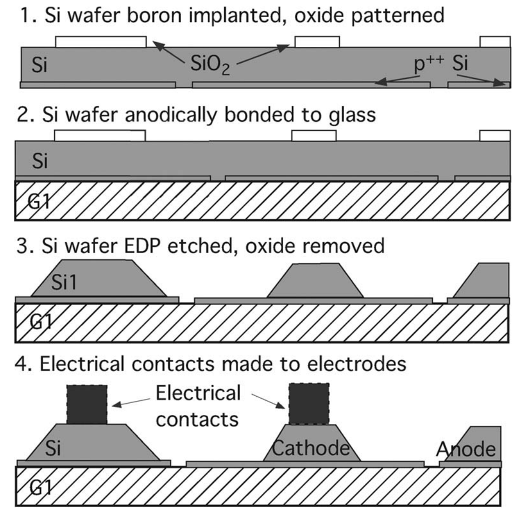

Fig. 3. Process flow of the SiG test structure. Masks 1 and 2 define a boron etch stop and a patterned oxide, respectively. Anodic bonding, followed by EDP etching, defines the cavity structure.

The use of metal electrodes with higher secondary electron emission coefficients (SEECs) can increase RF performance. The SEEC is defined as the number of ejected electrons per incident positive ion; these electrons trigger the avalanche process. Additionally, the composition and pressure of the gas in the discharge gap can impact the ease of ionization and the nature of the discharge current pulse, which can influence the radiated spectra. Hence, by tailoring the electrode material, operating pressure, and ratio of various fill gases (i.e., Ne and N_2), the RF performance can be controlled.

III. Fabrication

A. SiG Test Structure

The microstructure is fabricated in a simple two-mask process (Fig. 3) that includes a Si wafer and a glass wafer [8]. Beginning with a 500-μm-thick double-polished 1–10-$\Omega \cdot$cm $\langle 100 \rangle$ Si wafer, an oxide-masked boron diffusion (8 μm deep) is used to define the central cathode and the amplification region near the anode wall. The oxide is removed with a hydrofluoric acid dip. A second oxide mask on the backside of the wafer defines the footprint of the tapered anode. The Si wafer is aligned to the glass wafer (which is 500-μm-thick Pyrex #7740) and anodically bonded to it. The Si wafer is then subjected to a dopant-selective etch using ethylenediamine pyrocatechol (EDP) to form the cavity structures and expose the boron-doped cathodes and amplification regions.

A second glass layer (G2) normally caps the cavities. However, for the purpose of preliminary tests reported in this paper, the cavity structures are left unsealed and without the presence of the glass "cap" layer, which allows different fill-gas conditions to be evaluated. The test structure is then bonded to a standard high-voltage (HV) package. Fig. 4(a) shows a photograph of a composite die that has six separate test cavities on the microchip. Care was taken to isolate the test structure from the surrounding package by using an insulation material (mica) between the seat of the device and the package base.

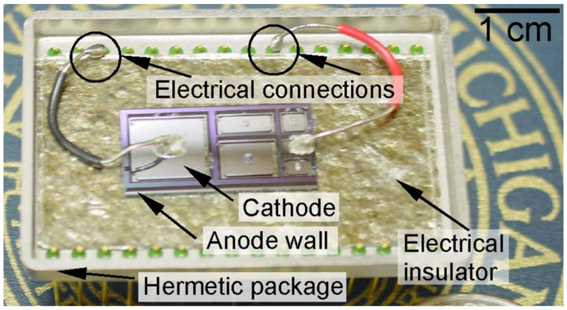

(a)

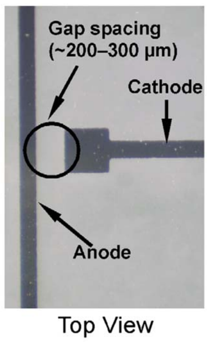

(b)

Fig. 4. (a) Photograph of the SiG microchip containing several different-sized test cavities. The 8×8 mm^2 cavity is shown to be bonded to a "plug-in"-style bathtub package (i.e., similar in type to Aegis, #PB114174EC100) that can be hermetically sealed. Electrical leads to the test structure were accomplished using a conductive epoxy, while connections to the package were soldered. (b) Photograph of the MOG test structure.

B. MOG Test Structure

The MOG test structure requires only one masking step. For the MOG (Cu), a Ti/Cu (50 nm/100 nm) seed layer is sputtered first on a 500-μm-thick Pyrex glass wafer. This is followed by a photopatterned electroplating mold for a 25-μm-thick Cu layer. The photoresist mold is then removed, and the base layers are etched away to form the structure [Fig. 4(b)]. The MOG (Ni) and MOG (Ir) test structures utilize thin-film electrodes (100 and 300 nm, respectively) that are formed by a lift-off process.

IV. Experimental Results

In order to understand the RF signaling that was generated by the electrical microdischarges in the presence of radiation sources, two types of measurements were conducted: wired and wireless. These measurements compared the microdischarges in the time and frequency domains. The impact of factors, such as electrode gap, gas species, and gas pressure, on discharge behavior was investigated. The test structures were also evaluated in the absence of radiation sources. In these tests, the microdischarges were stimulated electrostatically and by background radiation.

A. Experimental Setup

The test structures were placed in a larger test chamber that was filled with controlled mixtures of Ne/air, Ne/N_2, or air. For the wired measurements, a high-frequency (1-GHz) current probe was inductively coupled to the cathode and connected to a wideband oscilloscope (4 GSa/s). For the wireless measurements (shown in Fig. 5), tests were conducted inside an anechoic chamber that housed only the test structure and antenna. (The power supply and spectrum analyzer were located outside the chamber.) Table I summarizes the test conditions for each test. An HV dc power supply powered the test structure through a discharge circuit consisting of various passive components, such as ballast resistors and a bias capacitor. The drive circuit for the SiG and MOG test structures is shown in Fig. 5. For some tests that utilized the MOG structure, an external capacitor was not used. The capacitive element in the circuit diagram represents only the inherent capacitance of the electrodes ($\approx$ 1.1 pF). Each test structure was placed at specified distances from the sealed beta sources. The radiation sources were pure beta emitters, e.g., 0.1 μCi of ^{90}Sr and 1.0 μCi of ^{204}Tl. Beta particles directly interact with the fill gas with higher probability compared to gamma radiation.

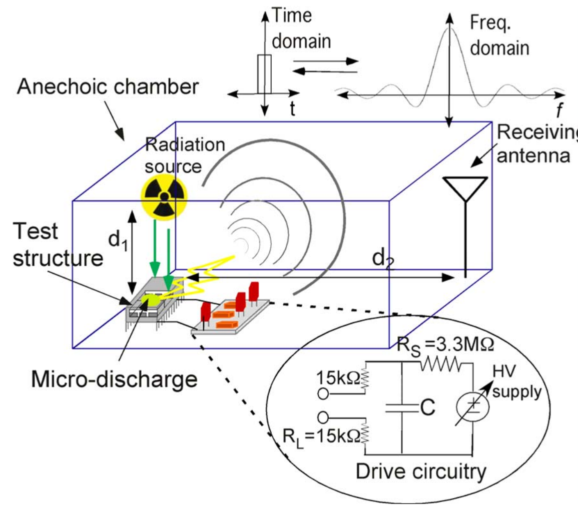

Fig. 5. Test setup showing the test structure and power circuitry positioned inside the anechoic chamber. When a beta source is present, the emitted particles initiate current microdischarges and consequent wireless transmission. The RF signal is measured by a receiving antenna connected to either a spectrum analyzer or an AM/FM radio. The radiation source-to-test structure distance (d_1) varied (up to 5 cm), as well as the antenna-to-test structure distance (d_2). Tests were operated in various gas environments, such as air, Ne/air mixture, and Ne/N_2 fill-gas environments. The applied voltage was between 800 and 1200 V.

B. MOG Test Structures

The MOG test structures were used to illustrate the impact of electrode spacing, pressure, and gas mixture. These measurements are collectively shown in Fig. 6 and Table II. Fig. 6 shows measurements for two MOG gap separations (165 and 235 μm) and two gas ratios of Ne and N_2 (10 : 1 and 25 : 1 volumetric ratios). Table II shows measurements for 235-μm electrode gaps and Ne:N_2 ratios of 1 : 5 to 3 : 5.

Consistent with Paschen's curve [29], the smaller electrode gap exhibited a smaller minimum operating potential compared to the larger electrode gap. The minimum operating voltage is the lowest voltage required to initiate a microdischarge in the presence of radiation. In addition, the electrostatically stimulated operating voltage (EOV) was observed to be higher

TABLE I
REFERENCE CHART OF THE VARIOUS TEST CONDITIONS ORGANIZED BY FIGURE NUMBER

Figure Number	Device Structure	Wired/Wireless Measurement	Antenna Type	Gas Type & Pressure	Discharge Initiation
5	MOG (Cu)	Wired	N/A	Ne/N_2 @ various pressures	Beta-initiated/ Electrostatic
6	SiG	Wired	N/A	Air @ 760 Torr	Electrostatic
8	SiG	Wireless	Whip	Ne/air @ 760 Torr	Beta-initiated
10	SiG	Wireless	Whip	Air @ 760 Torr	Electrostatic
11	MOG (Ir), SiG	Wireless	Log-Periodic	Air @ 760 Torr	Electrostatic
12	MOG (Ir, Cu)	Wireless	Whip	Various environments	Beta-initiated/ Electrostatic

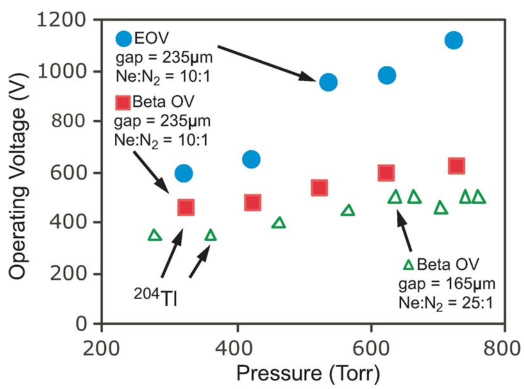

Fig. 6. Wired measurement. Operating voltages in the presence of 1.0 μCi of ^{204}Tl beta radiation (Beta OV), and EOV as a function of pressure and electrode gap. The $Ne:N_2$ gas ratio varied from 10 : 1 to 25 : 1. MOG (Cu) test structures were tested.

than the operating voltage in the presence of beta radiation (Beta OV).

As additionally expected from Paschen's curve, the minimum operating voltage increased with fill-gas pressure. This is illustrated, for example, by the plots for 235-μm electrode spacing in 10 : 1 $Ne:N_2$ (Fig. 6). (This suggests that packaging the device in partial vacuum can diminish the minimum operating voltage.)

Also expected from Paschen's curve [30], higher $Ne:N_2$ decreased the minimum operating potential. In Table II, for example, an increase in Ne content from 17% to 38% decreased the operating potential by 200 V. This is consistent with Fig. 6, where the Ne content was increased from 91% to 96%. (This lowering of minimum operating voltage may be attributed to the lower ionization potential of the monatomic gas [Ne (21.6 eV)] compared to the effective ionization potential of the diatomic gas [N_2 (32–38 eV)] [31].)

The impact of gas mixture on RF transmission was also evaluated. The "total received wireless power" was determined by summing the amplitudes of all frequency components of the RF spectra measured during current discharge activity. The spectra spanned the measurement bandwidth (0–4 GHz in 10-MHz intervals). The "total received background noise power" was determined similarly by summing the amplitudes of the measured RF spectra without current discharges present. This value limits the minimum detectable wireless signal. As shown in Table II, the signal-to-noise ratio of the received wireless power remained consistent regardless of the fill-gas mixtures evaluated and despite the changes in minimum operating voltage.

C. SiG Test Structures

Fig. 7 shows oscilloscope traces of the impulse-shaped current pulses from electrostatic discharges in the SiG microstructures. There are two components: a large primary discharge and smaller faster secondary discharges. The primary discharge is governed mainly by the RC time constant of the circuit (which is on the order of hundreds of microseconds in duration). The smaller secondary discharges are superimposed on the primary discharge (and are on the order of tens of nanoseconds in duration). As the bias capacitor is reduced from $C = 2$ nF to $C = 10$ pF, the primary discharge duration reduces until the primary and secondary pulses converge into a single current pulse.

These current pulses have an initial large peak with rise times on the order of 0.1–2 ns, which contribute to the wideband nature of the RF signal. Joint time–frequency analysis, particularly the short-time Fourier transform (STFT), can be used to evaluate how the frequency content of the signal changes with time. The STFT is determined by performing the Fourier transform on short sections of the time-domain signal. The spectrogram is an image representation of the STFT, where the x- and y-axes represent time and frequency, respectively, while the color denotes the signal intensity at that particular frequency and time. For example, Fig. 8(a) shows an expanded view of the current signal in Fig. 7. Fig. 8(b) shows the spectrogram of the current signal. The frequency content for the measured microdischarge signal extends into the gigahertz frequency range, with the majority of the signal intensity being concentrated at the initial peaks of the current signal.

The wireless spectrum was monitored using antennas coupled to a spectrum analyzer (Agilent ESA4405B). There were two types of receiving antennas used for the wireless measurements: a log-periodic antenna (EMCO 93146) and an 800-MHz whip antenna. The antenna gain factors (AGFs) were provided by the manufacturers (Fig. 9). The total received wireless power decreases with antenna-to-test structure distance (Fig. 10). Here, the total received wireless power was determined by summing the amplitudes of all frequency components spanning the measurement bandwidth (100–500 MHz in 0.833-MHz intervals). The measurements were performed in air as the fill gas at atmospheric pressure for an SiG test structure.

TABLE II
IMPACT OF FILL-GAS MIXTURE ON OPERATING VOLTAGE AND TOTAL RECEIVED WIRELESS POWER FROM 0 TO 4 GHz

Pressure = 737 Torr	Ratio of (Ne:N_2)		
Electrode gap[1] = 235 µm	1:5	2:5	3:5
Minimum operating voltage (V)	1400	1300	1200
Total received wireless power above background[2] (dBµV-MHz)	4412	4690	4155

[1]The MOG (Cu) test structures with 235 µm electrode gaps were tested.
[2]Total received background noise ≈214,350 dBµV-MHz.

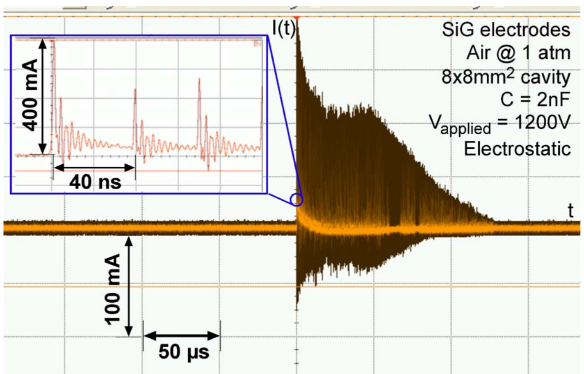

Fig. 7. Wired measurement. The current pulses from the SiG test structure are impulselike in shape. Within the primary discharge (hundreds of microseconds), there are many smaller secondary discharges (tens of nanoseconds) that also take place as shown. The microdischarges have an initial large peak with rise times on the order of 0.1–2 ns, which are thought to be responsible for generating the RF signal. A high-frequency (1-GHz) current probe inductively coupled to the cathode and connected to a wideband oscilloscope (4 GSa/s) was used to measure the electrostatically stimulated discharge.

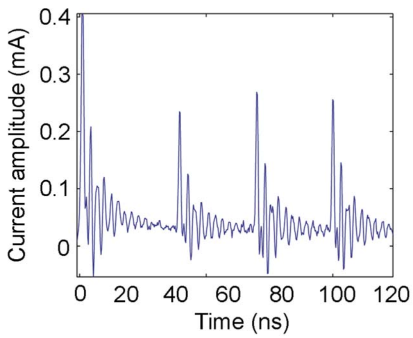

(a)

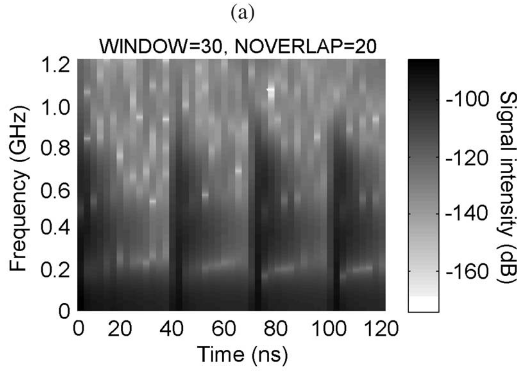

(b)

Fig. 8. (a) Four current pulses from wired measurements taken from Fig. 7 exhibit large initial peaks. (b) STFT of these pulses shows spectral content extending into the gigahertz frequency range that is concentrated at the beginning of each pulse and decays over time.

D. Comparisons of Test Structures

A comparison of the RF spectra generated by the SiG electrodes with the MOG (Ir) electrodes showed a good overall

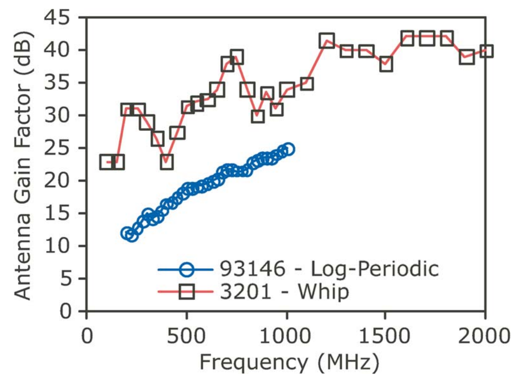

Fig. 9. AGFs supplied by the manufacturers for the 200-MHz–1.1-GHz log-periodic antenna (EMCO 93146) and the 800-MHz whip antenna used for this effort.

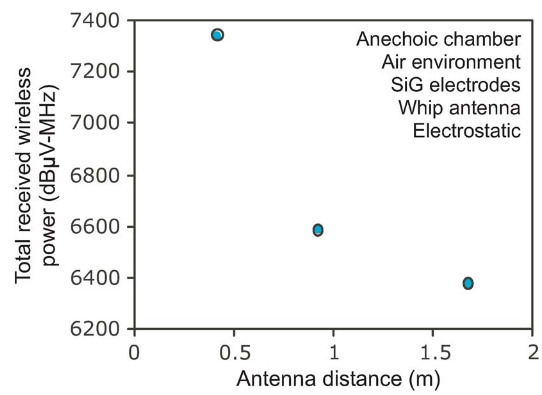

Fig. 10. Wireless measurement. The measured signal power (above background noise) attenuates as a function of antenna-to-test structure (SiG) distance (d_2). The total received wireless power is the sum of all measured frequency amplitudes from 100 to 500 MHz, taking into account the AGF. The total received background noise ≈ 21 767 dB · μV · MHz.

matching of the shape and amplitude (Fig. 11). The AGF and free-space loss (FSL) were taken into account in order to determine the generated RF signal at the transmission point (i.e., at the microstructure).

Fig. 12(a) shows the RF signal above the background noise spectrum from a MOG (Ir) device at 1.67 m. This measurement was taken in the absence of a radiation source, with air as the fill gas. Fig. 12(b) shows the reproducibility of the RF signal. It compares the above signal with other measured RF spectra from MOG (Cu) test structures. Each spectrum was measured with the same whip antenna but at different antenna-to-test structure distances, different times, and different locations. The AGF and FSL were taken into account for each spectrum in order to compare the generated spectra at the transmission point.

MOG test structures with nickel and copper electrodes (with identical metal patterns) show comparable minimum operating voltages at 760 torr (Table III). However, nickel electrodes

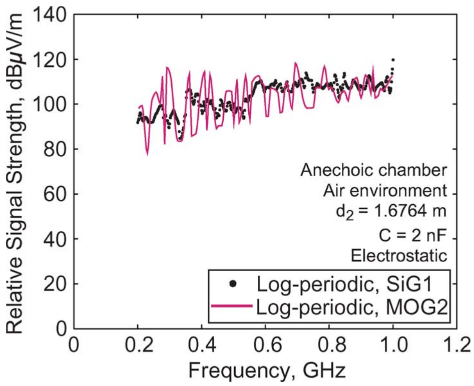

Fig. 11. Wireless measurement. A comparison of the RF spectra generated by the SiG electrodes with the MOG (Ir) electrodes showed similarities in shape and amplitude. The spectra were measured in an anechoic chamber with an antenna-to-test structure distance of 1.67 m. The AGF and FSL were taken into account.

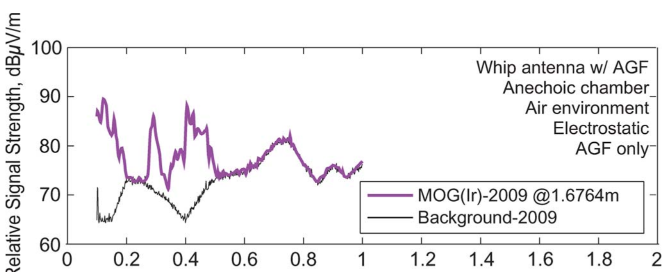

(a)

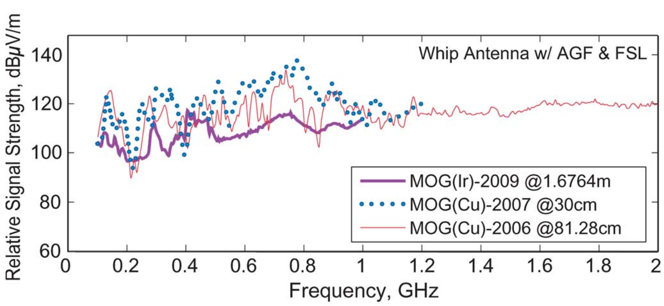

(b)

Fig. 12. Wireless measurement. (a) Generated RF signal above the background noise spectrum. The AGF was taken into account. (b) Signal reproducibility demonstrated using various MOG test structures at various times (spanning approximately three years) and locations (e.g., inside and outside the anechoic chamber). Also, each spectrum was taken at different distances. In order to account for this, the AGF and FSL were taken into account.

TABLE III
IMPACT OF ELECTRODE MATERIAL ON OPERATING VOLTAGE AND TOTAL RECEIVED WIRELESS POWER FROM 0 TO 4 GHz

Electrode Material[1]	Cu	Ni
Min. Operating Voltage (V)	700	750
Total received wireless power *above* background noise[2] (dBμV-MHz)	6664	8582

[1]MOG test structures with 235 μm electrode gaps. 0.1 μCi of ^{90}Sr.
[2]Total received background noise ≈127,786 dBμV-MHz.

provide an increase of approximately 30% in total received wireless power compared to copper electrodes. This is likely due to the higher SEEC of Ni (≈ 0.015) over Cu (≈ 0.01) [32].

To address the impact of using standard packages on the device performance, the RF spectra were measured with and

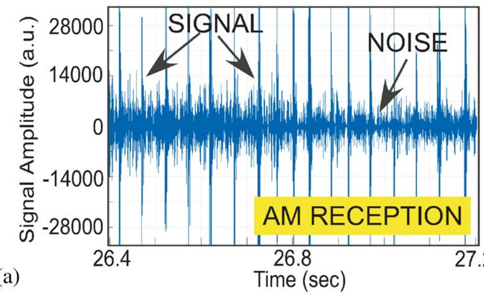

(a)

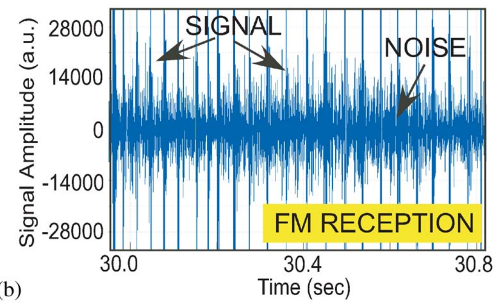

(b)

Fig. 13. Wireless measurement. Audio recordings received by an AM/FM radio: (a) AM recordings and (b) FM recordings at 108 MHz. The radiation source was ^{204}Tl, located 1 cm from the SiG test structure; the tip of the radio antenna was 7.6 cm away from the test structure. The length of the receiver antenna when fully extended is 56 cm. The audio tracings were visualized using the software program SIGVIEW, which plots signal intensity versus real time.

without the SiG test structure bonded to a package of the type and configuration shown in Fig. 4(a). There was minimal influence on the measured output spectra from the HV metal package. Also, there was no detectable impact on the RF performance from the type of beta source.

The RF signaling from the SiG test structures was also monitored using a commercially available AM/FM radio. The radio was positioned at distances greater than 50 cm from the SiG microstructure and received RF transmissions spanning the entire available AM (525–1705 kHz) and FM (88–108 MHz) bandwidths (Fig. 13). The length of the receiver antenna was 56 cm. For these measurements, the test structure was in a Ne/air environment near atmospheric pressure.

V. DISCUSSION AND CONCLUSION

A number of assessments can be made on the basis of the observations. First, while it is possible to initiate discharges in the absence of a radiation source, the bias must be elevated by about 50 V. This is dependent on background cosmic radiation and random thermal emission. The additional bias necessary to initiate electrostatic breakdown represents a noise margin.

Second, with respect to the oscilloscope traces of the electrostatic discharges from the SiG microstructures, the smaller secondary pulses are likely due to the charged particles crossing the electrode gap during the microdischarge. The physical mechanism involves charge buildup on the external capacitor during predischarge conditions, and during the discharge, the smaller secondary pulses bleed out this charge from the external capacitor until the potential on the capacitor is below the breakdown threshold of the discharge gap and the discharge is quenched.

Third, with respect to the radiated spectra, the parameters of the drive circuitry (Fig. 5) can have a significant impact on frequency response. For example, the bandwidth can be proportional to the load resistance (R_L, i.e., the resistance tied to the cathode) [18]. In addition, it has been observed that as the external capacitor, attached to a SiG test structure, decreases (e.g., from 22 nF to 10 pF), the radiated bandwidth and spectral content increases [27].

With respect to the audio recordings shown in Fig. 13, the periodicity of peaks (20–30 counts/s) is likely due to the microstructure drive circuitry. The detection rate is not likely to be limited by the radiation flux (1800–2000 disintegrations/s) but rather by the recovery time of the drive circuit. This is dominated by the charging time of the capacitor (15–20 ms) and also dependent upon factors, such as the local heating and cooling of the electrodes during the discharge process. Additionally, impurities in the fill-gas mixture can cause the recombination and neutralization process of the charged particles created during the avalanche process to be inefficient, and increase the dead time of the detector.

When comparing the two test structures presented here, several factors must be considered, such as ease of fabrication, electrode durability to microdischarges, and wireless transmission strength and distance. The wireless transmission capability of the two test structures was comparable (as seen in Fig. 11). However, the MOG test structures are typically easier to fabricate. Additionally, the electroplated metal electrodes, which have higher thermal conductance than Si electrodes, can be more durable under typical discharge conditions.

With the emergence of wireless sensor applications along with new wireless standards, distributed wireless sensing networks appear promising. For example, the FCC allocated the frequency range from 3.1 to 10.6 GHz for unlicensed UWB communication in 2002 [33]. Radiation sensors with an intrinsic wireless transmission capability offer an efficient and low-power mechanism for remote detection and networked monitoring. In this effort, the evaluation of wireless transmissions from radiation detector test structures has demonstrated bandwidths extending into the gigahertz frequency range and field strengths up to 90 dB $\cdot$ μV/m at 1.67 m. This range was constrained by the test conditions. For example, the antenna used to receive the transmissions was a general-purpose log-periodic antenna not customized for the nature of these transmissions. In the general case, the maximum separation distance between a signaling detector and a receiver will depend on the sensitivity and sophistication of the receiver. With appropriate design of both the receiver and the transmitter, transmission ranges on the order of 10 m are conceivable.

Acknowledgment

The authors would like to thank Dr. C. Wilson for the help with fabricating the SiG test structures and Prof. K. Sarabandi and Dr. A. Nashashibi for the access to the anechoic chamber and assistance in setting up the wireless measurements. The facilities used for this paper include the Michigan Nanofabrication Facility, University of Michigan, Ann Arbor.

References

[1] T. Masuzawa, M. Fujino, K. Kobayashi, T. Suzuki, and N. Kinoshita, “Wire electro-discharge grinding for micro-machining,” *Ann. CIRP*, vol. 34, no. 1, pp. 431–434, 1985.

[2] T. Masaki, K. Kawata, and T. Masuzawa, “Micro electro-discharge machining and its applications,” in *Proc. IEEE Int. Workshop MEMS*, Feb. 1990, pp. 21–26.

[3] K. Takahata and Y. B. Gianchandani, “Batch mode micro-electro-discharge machining,” *J. Microelectromech. Syst.*, vol. 11, no. 2, pp. 102–110, Apr. 2002.

[4] S. A. Wright and Y. B. Gianchandani, “Controlling pressure in microsystem packages by on-chip microdischarges between thin-film titanium electrodes,” *J. Vac. Sci. Technol. B, Microelectron. Nanometer Struct.*, vol. 25, no. 5, pp. 1711–1720, Sep./Oct. 2007.

[5] J. C. T. Eijkel, H. Stoeri, and A. Manz, “A DC microplasma on a chip employed as an optical emission detector for gas chromatography,” *Anal. Chem.*, vol. 72, no. 11, pp. 2547–2552, Jun. 2000.

[6] L. Que, C. G. Wilson, and Y. B. Gianchandani, “Microfluidic electrodischarge devices with integrated dispersion optics for spectral analysis of water impurities,” *J. Microelectromech. Syst.*, vol. 14, no. 2, pp. 185–191, Apr. 2005.

[7] B. Chua, A. Wexler, N. C. Tien, D. A. Niemeier, and B. A. Holmen, “Design, fabrication, and testing of a microfabricated corona ionizer,” *J. Microelectromech. Syst.*, vol. 17, no. 1, pp. 115–123, Feb. 2008.

[8] C. K. Eun, C. Wilson, and Y. B. Gianchandani, “A bulk silicon micromachined structure for gas microdischarge-based detection of beta-particles,” *J. Micromech. Microeng.*, vol. 18, no. 9, pp. 95 007–95 016, Sep. 2008.

[9] G. F. Knoll, *Radiation Detection and Measurement*. Hoboken, NJ: Wiley, 2000.

[10] F. Sauli, “Micro-pattern gas detectors,” *Nucl. Instrum. Methods Phys. Res. A, Accel. Spectrom. Detect. Assoc. Equip.*, vol. 477, no. 1–3, pp. 1–7, Jan. 2002.

[11] S. F. Biagi and T. J. Jones, “The microdot gas avalanche chamber: An investigation of new geometries,” *Nucl. Instrum. Methods Phys. Res. A, Accel. Spectrom. Detect. Assoc. Equip.*, vol. 361, no. 1/2, pp. 72–75, Jul. 1995.

[12] A. Oed, “Position-sensitive detector with microstrip anode for electron multiplication with gases,” *Nucl. Instrum. Methods Phys. Res. A, Accel. Spectrom. Detect. Assoc. Equip.*, vol. 263, no. 2/3, pp. 351–359, Jan. 1998.

[13] M. Wada, J. Suzuki, and Y. Ozaki, “Cadmium telluride β-ray detector,” in *Proc. IEEE Transducers*, 1987, vol. A478, pp. 258–261.

[14] G. Charpak, J. Derre, Y. Giomataris, and P. Rebourgeard, “Micromegas, a multipurpose gaseous detector,” *Nucl. Instrum. Methods Phys. Res. A, Accel. Spectrom. Detect. Assoc. Equip.*, vol. 478, no. 1/2, pp. 26–36, Feb. 2002.

[15] H. Nishimura, K. Hattori, S. Kabuki, H. Kubo, K. Miuchi, T. Nagayoshi, Y. Okada, R. Orito, H. Sekiya, A. Takada, T. Tanimori, K. Tsuchiya, and K. Ueno, “The performance of the micro time projection chamber based on μ-PIC,” in *Conf. Rec. IEEE Nucl. Sci. Symp.*, Oct. 2006, vol. 6, pp. 3860–3864.

[16] C. Son and B. Ziaie, “Electret based wireless micro ionizing radiation dosimeter,” in *Proc. IEEE Int. Conf. MEMS*, Jan. 2006, pp. 610–613.

[17] J. D. Jackson, *Classical Electrodynamics*. New York: Wiley, 1999.

[18] W. Janischewskyj, A. M. Hussein, and N. H. C. Santiago, “Performance and analysis of a micro-gap discharge circuit,” *IEEE Trans. Power Del.*, vol. 3, no. 2, pp. 694–706, Apr. 1988.

[19] P. F. Wilson and M. T. Ma, “Fields radiated by electrostatic discharges,” *IEEE Trans. Electromagn. Compat.*, vol. 33, no. 1, pp. 10–18, Feb. 1991.

[20] M. Mardiguian, “Comments on ‘Fields radiated by electrostatic discharges’,” *IEEE Trans. Electromagn. Compat.*, vol. 34, no. 1, p. 62, Feb. 1992.

[21] J. E. Brittain, “Electrical engineering Hall of Fame: Guglielmo Marconi,” *Proc. IEEE*, vol. 92, no. 9, pp. 1501–1504, Sep. 2004.

[22] A. G. Heaton and J. H. Reeves, “Microwave radiation from discharges,” in *Proc. 3rd Int. Conf. Gas Discharges*, Sep. 1974, pp. 73–77.

[23] L. L. Altgilbers, V. A. Somov, I. Chepurniy, Y. V. Tkach, and A. O. Silin, “Broadband pulsed generator based on H-waveguide,” in *Proc. 14th IEEE Int. Pulsed Power Conf.*, 2003, vol. 2, pp. 1173–1176.

[24] R. J. Nemzek, J. S. Dreicer, D. C. Torney, and T. T. Warnock, “Distributed sensor networks for detection of mobile radioactive sources,” *IEEE Trans. Nucl. Sci.*, vol. 51, no. 4, pp. 1693–1700, Aug. 2004.

[25] R. Kyker, N. Berry, D. Stark, N. Nachtigal, and C. Kershaw, “Hybrid Emergency Radiation Detection (HERD), a wireless sensor network application for consequence management of a radiological release,” in *Proc. SPIE*, 2004, vol. 5440, pp. 293–304.

[26] C. K. Eun, R. Gharpurey, and Y. B. Gianchandani, "Broadband wireless sensing of radioactive chemicals utilizing inherent RF transmissions from pulse discharges," in *Proc. IEEE Conf. Sensors*, Nov. 2005, pp. 273–276.
[27] C. K. Eun, R. Gharpurey, and Y. B. Gianchandani, "Controlling ultra wide band transmissions from a wireless micromachined Geiger counter," in *Proc. IEEE Int. Conf. Micro Electro Mech. Syst.*, Jan. 2006, pp. 570–573.
[28] C. K. Eun and Y. B. Gianchandani, "Exploring RF transmissions from discharge-based micromachined radiation detectors," in *Proc. IEEE Conf. Technol. Homeland Security*, May 2008, pp. 18–23.
[29] F. Paschen, "Ueber die zum Funkenübergang in Luft, Wasserstoff und Kohlensäure bei verschiedenen Drucken erforderliche Potentialdifferenz," *Ann. Phys.*, vol. 273, no. 5, pp. 69–96, 1889.
[30] Y. P. Raizer, *Gas Discharge Physics*. New York: Springer-Verlag, 1997.
[31] U. Yusupaliev, "Stoletov constant and effective ionization potential of a diatomic gas molecule," *Bull. Lebedev Phys. Inst.*, vol. 34, no. 11, pp. 334–339, Nov. 2007.
[32] P. Guillot, P. Belenguer, L. Therese, V. Lavoine, and H. Chollet, "Secondary electron emission coefficients of standard samples for GDOES," *Surf. Interface Anal.*, vol. 35, no. 7, pp. 590–592, Jul. 2003.
[33] "FCC 02-48, First Report and Order," Revision of Part 15 of the Commission's Rules Regarding Ultra-Wideband Transmission Systems, Feb. 14, 2002. [Online]. Available: http://hraunfoss.fcc.gov/edocs_public/attachment/FCC-02048A1.pdf

Christine K. Eun received the B.S. and M.S. degrees from the University of Michigan, Ann Arbor, in 2004 and 2006, respectively, where she is currently working toward the Ph.D. degree in electrical engineering, with a focus on MEMS and radiation detection, in the Department of Electrical Engineering and Computer Science.

Ranjit Gharpurey received the B.Tech. degree from the Indian Institute of Technology, India, in 1990 and the Ph.D. degree in electrical engineering from the University of California, Berkeley, in 1995.

He was with Texas Instruments Incorporated from 1995 to 2003 and with the Department of Electrical Engineering and Computer Science, University of Michigan, Ann Arbor, from 2003 to 2005. He is currently an Associate Professor with the Department of Electrical and Computer Engineering, University of Texas, Austin. His research interests are in the area of RF and analog circuit design, including circuits and architectures for wireless communication applications, interference detection and cancellation in wireless systems, low-power and low-voltage analog circuit design, and noise mechanisms related to circuit activity. He has authored or coauthored numerous peer-reviewed journal and conference papers. He has coauthored a book on the subject of substrate coupling in integrated circuits and has also edited a book entitled *Ultra Wideband Circuits, Transceivers, and Systems*. He is a holder or coholder of over 20 patents granted by the United States Patent and Trademark Office.

Dr. Gharpurey is currently an Associate Editor for the IEEE JOURNAL OF SOLID-STATE CIRCUITS and serves on the Technical Program Committees of the International Solid-State Circuits Conference and the Radio Frequency Integrated Circuits Symposium.

Yogesh B. Gianchandani (S'83–M'85–SM'04) received the B.S., M.S., and Ph.D. degrees in electrical engineering, with a focus on microelectronics and MEMS.

He is presently a Professor at the University of Michigan, Ann Arbor, with a primary appointment in the Electrical Engineering and Computer Science Department and a courtesy appointment in the Mechanical Engineering Department. His research interests include all aspects of design, fabrication, and packaging of micromachined sensors and actuators and their interface circuits (http://www.eecs.umich.edu/~yogesh/). He has published approximately 200 papers in journals and conferences, and has about 30 U.S. patents issued or pending. He was a Chief Co-Editor of *Comprehensive Microsystems: Fundamentals, Technology, and Applications*, published in 2008. He serves several journals as an editor or a member of the editorial board, and served as a General Co-Chair for the IEEE/ASME International Conference on Micro Electro Mechanical Systems (MEMS) in 2002. From 2007 to 2009, he also served at the National Science Foundation as the Program Director for Micro and Nano Systems within the Electrical, Communication, and Cyber Systems Division.